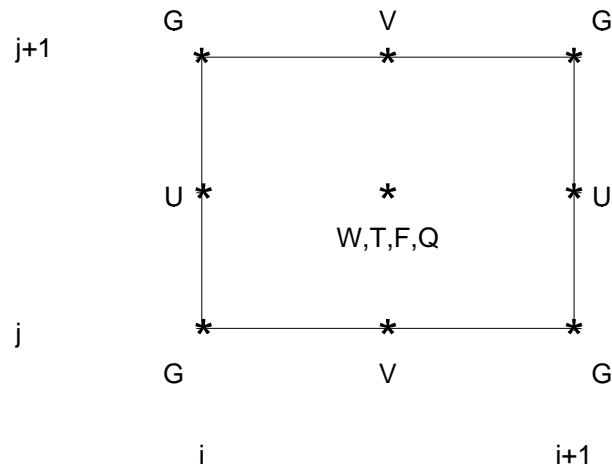# Institut Pierre Simon Laplace
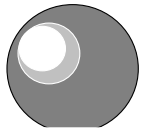## des Sciences de l'Environnement Global

Notes du Pôle de Modélisation

The Trident Pacific model. Part 1: The oceanic dynamical model and observations during the TOPEX/POSEIDON period

Jean-Philippe Boulanger

IPSL - Laboratoire d'Océanographie Dynamique et de Climatologie

Janvier 2000   **Note n° 16**

The present study aims to extend the qualitative description of the 1997-1998 El Niño event presented in a recent paper by Boulanger and Menkes (1999) by bringing a more quantitative estimate of the role of long equatorial waves and their reflection. Toward that end, the Trident model is developped to better understand dynamical and thermodynamical mechanisms induced by long equatorial waves in the equatorial Pacific. In this first paper, the model dynamics are described and validated. The oceanic model dynamics are derived from a linear 3-1/2 layer model. The surface layer (mixed-layer) has a constant depth. Therefore the three active layer model is equivalent to considering a shear layer solution and two baroclinic modes. Contrary to other similar models which use a weak linear Rayleigh friction, a quadratic friction (applied in the momentum equations) is shown to allow a fair representation of both the phase and amplitude of the sea level and the zonal currents in the equatorial Pacific. When the model is run with a strong linear Rayleigh friction ((6 months)-1), it deviates more from the observations, and the variability in the western Pacific is overestimated as the Rossby waves are not sufficiently damped as they propagate westward. Other sensitivity experiments are discussed: in particular the model-data comparisons are not very sensitive to the number of baroclinic modes considered with comparable results to when only one baroclinic mode is used; on the other hand, we found a large sensitivity to friction with large improvement when a quadratic friction is used. Finally, it is shown that simple ocean models using a weak linear Rayleigh friction poorly simulate equatorial zonal surface currents whether they include one or more baroclinic modes. It is concluded that this linear representation of friction in such linear models is not suitable to study the respective roles of thermocline displacement and zonal advection on ENSO time scales.

Janvier 2000
Note n° 16

The Trident Pacific model.

Part 1: The oceanic dynamical model and observations during the

TOPEX/POSEIDON period

Jean-Philippe Boulanger*

*Laboratoire d'Océanographie Dynamique et de Climatologie
UMR CNRS/ORSTOM/UPMC
Université Pierre et Marie Curie
Tour 26/Etage 4/Case100
4 Place Jussieu
75252 Paris, Cedex 05
France
E-mail: jpb@lodyc.jussieu.fr

Abstract

The present study aims to extend the qualitative description of the 1997-1998 El Niño event presented in a recent paper by Boulanger and Menkes (1999) by bringing a more quantitative estimate of the role of long equatorial waves and their reflection. Toward that end, the Trident model is developped to better understand dynamical and thermodynamical mechanisms induced by long equatorial waves in the equatorial Pacific. In this first paper, the model dynamics are described and validated. The oceanic model dynamics are derived from a linear 3-1/2 layer model. The surface layer (mixed-layer) has a constant depth. Therefore the three active layer model is equivalent to considering a shear layer solution and two baroclinic modes. Contrary to other similar models which use a weak linear Rayleigh friction, a quadratic friction (applied in the momentum equations) is shown to allow a fair representation of both the phase and amplitude of the sea level and the zonal currents in the equatorial Pacific. When the model is run with a strong linear Rayleigh friction ((6 months)$^{-1}$), it deviates more from the observations, and the variability in the western Pacific is overestimated as the Rossby waves are not sufficiently damped as they propagate westward. Other sensitivity experiments are discussed: in particular the model-data comparisons are not very sensitive to the number of baroclinic modes considered with comparable results to when only one baroclinic mode is used; on the other hand, we found a large sensitivity to friction with large improvement when a quadratic friction is used. Finally, it is shown that simple ocean models using a weak linear Rayleigh friction poorly simulate equatorial zonal surface currents whether they include one or more baroclinic modes. It is concluded that this linear representation of friction in such linear models is not suitable to study the respective roles of thermocline displacement and zonal advection on ENSO time scales.

I. Introduction

In a recent study, Boulanger and Menkes (1999) investigated the reflection of Kelvin and Rossby waves at both the eastern and western boundaries using TOPEX/POSEIDON data during the 1992-1998 period. After showing evidences of reflection occuring at both boundaries during the entire period, they discussed potential mechanisms at work during the 1997-1998 El Niño event. The main goal of the present study (Part 1 and Part 2) is to offer a more quantitative description of the processes involved during the 1997-1998 strong El Niño event followed by La Niña by understanding the detailed mechanisms by which long equatorial waves contributed to the ENSO variability.

In order to understand the potential role of long equatorial waves and their reflection, a simple ocean model enables the estimation of the respective roles of wind-forced and reflected waves on ENSO time scales. Such models already exist (Zebiak and Cane, 1987; Chen et al., 1995; Dewitte, 1999). Unfortunately, despite the skill of these models in simulating the Niño3 index, none of these models have been thoroughly evaluated against recent oceanic observations of the tropical Pacific such as TOPEX/POSEIDON sea level data or Tropical Ocean Global Atmosphere - Tropical Atmosphere Ocean Array (Hayes et al., 1991; McPhaden, 1993) equatorial zonal currents. However, such a comparison is necessary in order to gain confidence in model deduced mechanisms. The objective of the present study is to investigate the potential role of long wave reflection through thermocline displacement and zonal advection. Therefore such a validation to data and the investigation of the model sensitivity are required. This objective has led to design a new oceanic (dynamical and thermodynamical) model of the Pacific ocean called Trident. In this first paper, only the oceanic dynamics is described and compared to observations. Briefly, the oceanic dynamics is derived from a linear 3-1/2 layer model, with a constant surface

layer (mixed-layer). Fluxes of mass and momentum are allowed between the first and second layers. As the surface layer has a constant depth, only two baroclinic modes exist in the model.

The two major parameters of this oceanic model are the intensity and the form of the friction applied onto the baroclinic equations and the number of baroclinic modes considered. First, although most of the models (Zebiak and Cane, 1987; Battisti, 1988; Chen et al., 1995; Picaut et al., 1997) use a weak linear Rayleigh friction, various model-data comparisons (Picaut et al., 1993; Kessler and McPhaden, 1995; Boulanger and Fu, 1995) have concluded that simple models perform better in simulating sea level when a strong Rayleigh friction is used. However, when such models use a strong friction they do not oscillate at ENSO period when coupled to a simple atmospheric model (Picaut et al., 1997; C. Perigaud, personal communication). Second, it is currently argued that, when using a weak Rayleigh friction, simple models simulate better the equatorial surface currents when more than one baroclinic mode is considered (Chen et al., 1995; Dewitte et al., 1999). Unfortunately, none of these studies have quantified the improvement by comparing the simulated fields to data such as the TAO zonal current observations. That comparison to data is performed in the present paper by evaluating the model skill in simulating both sea level and equatorial zonal currents when the model is run with different frictions and with one or two baroclinic modes.

This paper is organized as follows. Section 2 presents the various data (TOPEX/POSEIDON sea level, zonal currents from the Tropical Atmosphere Ocean Array, ERS+TAO surface wind stress data). Section 3 describes the model equations, grids and discretisation schemes. Section 4 discusses the comparison of the oceanic model dynamics to data and its simulated variability during the 1992-1998 period. Section 5 discusses the model

sensitivity to major parameters. Finally, Section 6 discusses the results and gives some conclusions.

II. Data

TOPEX/POSEIDON sea level data. The TOPEX/POSEIDON sea level data used in the present study are provided by the Center of Space Research at the University of Texas. A detailed description of the data processing and error analysis can be found in Tapley et al. (1994). The sea level data gridded on a 1°longitude by 1° latitude regular grid for each cycle are averaged onto the model grid. Data are monthly averaged. We use the first 230 cycles for the period October 1992-December 1998. Sea level anomalies are computed relative to the January 1993-December 1996 period, which showed very weak interannual variability (Boulanger and Menkes, 1998). Zonal geostrophic currents were derived as described in Menkes et al. (1995), and comparison to TAO data will be presented in Section IV.

TOGA-TAO zonal current data. One of the great achievements of the TOGA-TAO Array is to provide long time series of current profiles at different locations along the equator (mainly 110°W, 140°W, 165°E and 156°E). At these sites in-situ currents are measured with six to seven vector averaging current meters (VACMs) and/or with ADCP. Both kinds of measurements are highly correlated (McPhaden and McCarty, 1992). In cases when both measurements were available, ADCP observations were preferred. All data at each mooring location were monthly averaged. Data were then processed as follows. First, following methods described in McPhaden and McCarty (1992), missing data at a certain level were either interpolated (when close upper and lower levels were available) or extrapolated (when only one level was available) through either bilinear or linear regression. Only currents at 10-meter are used in the present study.

ERS wind stress data. ERS-1 and ERS-2 wind data were provided by the Centre ERS d'Archivage et de Traitement located in the Institut Français de Recherche pour l'Exploitation de la Mer. The method used to convert the radar backscatter measured by the ERS-1 and ERS-2 scatterometers is described and validated in Bentamy et al. (1996). The original product is gridded on a 1° longitude by 1° latitude regular grid and is a weekly average wind stress field. A recent study (Menkes et al., 1998) has highlighted the weak amplitude of the ERS wind stress in comparison to TAO wind data, leading to the choice of using the ERS+TAO wind stress data set constructed by Menkes et al. (1998). Data are monthly averaged and interpolated onto the model grid (2° longitude x 0.5° latitude). ERS-1 data were used from May 1992 to May 1996 while ERS-2 data were used from June 1996 to December 1998. A climatology was computed over the period January 1993-December 1996. Wind stress anomalies are computed relative to that period.

III. The oceanic model dynamics

The oceanic basin extends from 130°E to 80°W in longitude and from 20.25°S to 20.25°N in latitude. The grid resolution is 2° in longitude and 0.5° in latitude. The resolution is the same in each layer. The basin geometry is the one displayed in Figure 1. The model grid is displayed in Figure 2. It is similar to the Cane and Patton (1984) grid for the dynamics, and it is a C-grid (Arakawa, 1966) for the SST equation (Boulanger and Menkes, 1999b). It is important to note that contrary to the Zebiak and Cane (1987) or Chen et al. (1995) models, which have a coarse resolution for the SST equation with no equatorial point, the TRIDENT model resolution is the same for the dynamics and SST fields.

The model dynamics is derived from a 3-1/2 layer linear model (although the model can be also run with two layers). In such a model, the equations for each layer k is written :

$$\begin{cases} \partial_t u_k - \beta y v_k + \partial_x\left(p_k/\rho_0\right) = \dfrac{\tau^x_{k-1} - \tau^x_k}{\rho_0 H_k} + \text{Fric}(u_k) \\[2ex] \partial_t v_k + \beta y u_k + \partial_y\left(p_k/\rho_0\right) = \dfrac{\tau^y_{k-1} - \tau^y_k}{\rho_0 H_k} + \text{Fric}(v_k) \\[2ex] \partial_t h_k + H_k\left(\partial_x u_k + \partial_y v_k\right) = -\left(w_{k-1} - w_k\right) + \text{Fric}(h_k) \end{cases}$$

where $u_k, v_k, w_k, h_k, H_k, p_k, \tau^x_k, \tau^y_k$ respectively represent the zonal, meridional, and vertical current components, the anomalous layer thickness, the mean thickness, the anomalous layer pressure, and the zonal and meridional stress components between the layers k and k+1. At the surface, τ^x_0 and τ^y_0 are the zonal and meridional wind stresses, and w0=0. Frictional terms are also considered, their analytical form will be discussed later in the paper.

The following hypotheses are made:

(i) the first layer (mixed-layer) has a constant depth i.e. the anomalous layer thickness and pressure verify h1=0 and p1=p2

(ii) the interface between the first and second layer is not a material surface i.e. there are fluxes of mass and momentum through the interface

(iii) the interface between the second and third layer (representative of the top of the thermocline) is considered as a material surface with no flux through the interface

Introducing (uS, vS) as the shear currents between the first and second layers, the difference between the momentum equations of the surface layer with the momentum equations of the second layer leads to the following equations:

$$\begin{cases} \partial_t u_s - \beta y v_s = \dfrac{\tau_0^x}{\rho_0 H_1} - \dfrac{\tau_1^x}{\rho_0}\left(\dfrac{1}{H_1} + \dfrac{1}{H_2}\right) + \mathrm{Fric}(u_1) - \mathrm{Fric}(u_2) \\[2mm] \partial_t v_s + \beta y u_s = \dfrac{\tau_0^y}{\rho_0 H_1} - \dfrac{\tau_1^y}{\rho_0}\left(\dfrac{1}{H_1} + \dfrac{1}{H_2}\right) + \mathrm{Fric}(v_1) - \mathrm{Fric}(v_2) \\[2mm] \qquad w_s = H_1\left(\partial_x u_s + \partial_y v_s\right) \end{cases}$$

$\vec{\tau}_1/\rho_0$ is taken as a vertical diffusion term at the base of the mixed-layer i.e.

$\vec{\tau}_1/\rho_0 = \left(K\partial_z \vec{u}\right)_{z=-H_1} = K\vec{u}_s/H_1 = K_u \vec{u}_s$. The coefficient $K_u H_1$ has a value chosen as $3.25.10^{-3}\ \mathrm{m}^2.\mathrm{s}^{-1}$.

Such a coefficient is similar to values of vertical mixing in the mixing layer (Blanke and

Delecluse, 1993) but is large compared to values at the base of the mixing layer. Actually, this

term represents the transfer of momentum from the surface to the base of the mixing layer i.e. it

includes the effect of vertical mixing and of entrainment/detrainment related to the vertical

displacement of the mixed-layer, a mechanism not explicitly simulated by the model. For the sake

of simplicity this value is constant in time and space. Finally, a horizontal Laplacian diffusion is

taken into account when solving the shear layer equations. The horizontal diffusion coefficient is

chosen as $2000\mathrm{m}^2.\mathrm{s}^{-1}$ except near the western boundaries where this value becomes $40000\mathrm{m}^2.\mathrm{s}^{-1}$. It also slowly increases from 2000 in the 10°N-10°S band up to 40000 at the northern and

southern boundaries (20°). Therefore, the final equations for the shear-layer are:

$$\begin{cases} \partial_t u_s - \beta y v_s = \dfrac{\tau_0^x}{\rho_0 H_1} - \dfrac{\tau_1^x}{\rho_0}\left(\dfrac{1}{H_1} + \dfrac{1}{H_2}\right) + K_H \Delta_H u_S + \mathrm{Fric}(u_1) - \mathrm{Fric}(u_2) \\[2mm] \partial_t v_s + \beta y u_s = \dfrac{\tau_0^y}{\rho_0 H_1} - \dfrac{\tau_1^y}{\rho_0}\left(\dfrac{1}{H_1} + \dfrac{1}{H_2}\right) + K_H \Delta_H v_S + \mathrm{Fric}(v_1) - \mathrm{Fric}(v_2) \\[2mm] \qquad w_s = H_1\left(\partial_x u_s + \partial_y v_s\right) \end{cases}$$

Now, we are interested in showing how the subsurface layer equations are solved using the

equivalence between a layer formulation and a baroclinic mode formulation. Considering the

following points: (i) $w_1 = w_s + H_1(\partial_x u_2 + \partial_y v_2)$, (ii) the subsurface dynamics at low frequency is mainly dominated by long Kelvin and Rossby waves (i.e. the system can be reduced using the long wave approximation), the subsurface layer equations can be rewritten:

$$\begin{cases} \partial_t u_k - \beta y v_k + \partial_x(p_k/\rho_0) = F_k \\ \qquad +\beta y u_k + \partial_y(p_k/\rho_0) = G_k \\ \partial_t h_k + H_k'(\partial_x u_k + \partial_y v_k) = Q_k \end{cases}$$

where $H_2' = H_1 + H_2$, $H_3' = H_3$ and the right-hand side terms are the sum of the forcing terms (momentum and mass fluxes) and frictional terms which form will be discussed later :

$$\begin{cases} F_k = \dfrac{\tau_1^x}{\rho_0 H_k'}\delta_{2k} + \text{Fric}(u_k) \\ G_k = \dfrac{\tau_1^y}{\rho_0 H_k'}\delta_{2k} + \text{Fric}(v_k) \\ Q_k = -w_s\delta_{2k} + \text{Fric}(h_k) \end{cases}$$

where $\delta_{ij} = 1$ if i=j and $\delta_{ij} = 0$ otherwise. The frictional terms are considered in the right-hand side of the equations, andwhen discretizing the model equations, they are explicit in time.

Then, introducing the matrix **A** relating h and p,

$$\mathbf{A} = \begin{pmatrix} 1/(g_{32}'H_2') & -1/(g_{32}'H_2') \\ -1/(g_{32}'H_3') & g_{42}'/(g_{43}'g_{32}'H_3') \end{pmatrix} = \begin{pmatrix} a_{11} & a_{12} \\ a_{21} & a_{22} \end{pmatrix}$$

where $g_{ij}' = g(\rho_j - \rho_i)/\rho_0$, and following the same notations as in McCreary et al. (1992), the subsurface layer equations can be written:

$$\begin{cases} \partial_t\mathbf{u} - \beta y\mathbf{v} + \partial_x(\mathbf{p}/\rho_0) = \mathbf{F} \\ \qquad \beta y\mathbf{u} + \partial_y(\mathbf{p}/\rho_0) = \mathbf{G} \\ \mathbf{A}\partial_t(\mathbf{p}/\rho_0) + (\partial_x\mathbf{u} + \partial_y\mathbf{v}) = \mathbf{Q} \end{cases}$$

where $\mathbf{q} = \begin{pmatrix} q_2 \\ q_3 \end{pmatrix}$ represents the zonal or meridional current, the pressure anomalies, the zonal or

meridional stress or the entrainment velocity in each subsurface layer. The solution to the two

layer system can be actually represented as expansions in the two baroclinic (vertical normal)

modes: $\mathbf{q} = q_1 \mathbf{\psi}_1 + q_2 \mathbf{\psi}_2$ where the eigenvectors and eigenvalues of the matrix $\mathbf{A}$ are respectively

$$\mathbf{\psi}_n = \begin{pmatrix} 1 \\ (\lambda_n - a_{11})/a_{12} \end{pmatrix} \text{ and } \lambda_n = c_n^{-2} = \frac{1}{2}\left[(a_{11} + a_{22}) + (-1)^n \left[(a_{11} - a_{22})^2 + 4a_{12}a_{21} \right]^{1/2} \right].$$ Introducing

the eigenvectors $\hat{\mathbf{\psi}}_n = \begin{pmatrix} 1 \\ (\lambda_n - a_{11})/a_{21} \end{pmatrix}$ of the adjoint matrix of $\mathbf{A}$, we can define a scalar product

such that $\langle \mathbf{q} | \mathbf{\psi}_n \rangle = q_1 \overline{\mathbf{\psi}}_1 \hat{\mathbf{\psi}}_n + q_2 \overline{\mathbf{\psi}}_2 \hat{\mathbf{\psi}}_n$ where $\overline{\mathbf{\psi}}_n = \begin{pmatrix} 1 & (\lambda_n - a_{11})/a_{12} \end{pmatrix}$. The norm of the

eigenvector n is then $\gamma_n = \langle \mathbf{\psi}_n | \mathbf{\psi}_n \rangle = \overline{\mathbf{\psi}}_n \hat{\mathbf{\psi}}_n = 1 + (\lambda_n - a_{11})^2/(a_{12}a_{21})$. Thus the system of

equations for each baroclinic mode (k=1, 2) is:

$$\begin{cases} \partial_t u_k - \beta y v_k + \partial_x(p_k/\rho_0) = F_k \\ \qquad\quad +\beta y u_k + \partial_y(p_k/\rho_0) = G_k \\ \partial_t(p_k/\rho_0) + \lambda_k^{-1}(\partial_x u_k + \partial_y v_k) = Q_k/\lambda_k \end{cases}$$

with $q_k = \langle \mathbf{q} | \mathbf{\psi}_k \rangle / \langle \mathbf{\psi}_k | \mathbf{\psi}_k \rangle = (q_2 + q_3 (\lambda_k - a_{11})/a_{21})/\gamma_k$. Therefore it comes that the ratio of

upper layer to lower layer variables for each mode k is $r_k = a_{12}/(\lambda_k - a_{11})$.

The solutions of each system of baroclinic equations is then solved using the model

described in Appendix A. The horizontal currents and the thickness anomalies of the subsurface

layers are then computed from the combination of the baroclinic solutions. The surface currents

are the sum of the shear currents and of the second layer currents. The sea level anomalies are

then computed following:

$$\eta = \sum_{n=2}^{3} h_n (\rho_4 - \rho_n)/\rho_0 = p_2/\rho_0$$

Frictional terms. The frictional terms (applied to the layer equations) can have two forms:

- the linear Rayleigh formulation

$$\begin{cases} \text{Fric}(u_k) = -r_k^u u_k \\ \text{Fric}(v_k) = -r_k^v v_k \\ \text{Fric}(h_k) = -r_k^h h_k \end{cases}$$

- a quadratic friction on the momentum, a linear friction on the layer thickness

$$\begin{cases} \text{Fric}(u_k) = -r_k^u u_k |u_k| \\ \text{Fric}(v_k) = -r_k^v v_k |v_k| \\ \text{Fric}(h_k) = -r_k^h h_k \end{cases}$$

The choice of such a formulation is motivated by two main reasons. First, the sea level variability is fairly well explained by linear dynamics. As a consequence, it is preferred to consider a linear friction on the layer thickness equations. Second, as will be shown in section 5, surface currents computed by a linear model using the linear Rayleigh formulation have a larger amplitude than observed surface currents. Indeed, non-linearities in the ocean play a major role in the current amplitudes. This is such an effect which is sought after by using a quadratic friction in the momentum equations. Although this formulation helps in constraining the model current amplitudes near the equator, it will induce an underestimation of the NECC where non-linearities might actually strengthen its amplitude (easward currents in a region of negative zonal current gradient).

As a final comment, it is important to note that this model is designed to study the role of long equatorial waves in ENSO events. As a consequence, this simplified oceanic model does not include many other mechanisms which can also play a major role on ENSO variability such as a variable mixed-layer depth (Chen et al., 1994), mean currents, a retroaction of the thermodynamics on the model dynamics and non-linearities.

IV. Evaluation and variability of the oceanic model dynamics

The control experiment described in this section is forced by the ERS+TAO wind stress product presented in Section II. The period extends from May 1992 to December 1998. Each simulation is preceded by a 5-year spin-up using the 1993-1996 wind stress climatology. Model outputs are monthly averaged. The model monthly outputs for this reference simulation (see Table 1 for the parameter description) are now compared to T/P sea-level and TAO surface current data.

Comparison with T/P sea-level data. Figure 3 displays the comparison between the simulated and observed sea-level variability during the period January 1993-December 1998. Statistics are summarized in Table 2. The main patterns of T/P sea level variability (Fig. 3a) are characterized by large amplitudes (higher than 8cm) over most of the equatorial eastern Pacific, and in the off-equatorial western Pacific. An equatorial minimum (less than 7cm) is observed in the region of interannual wind variability (170°E-160°W). The simulated sea level (Fig. 3b) has a similar amplitude as T/P data (Fig. 3a) in the equatorial eastern Pacific. In the western Pacific, the model displays too large a variability near 5°S. In the Northern Hemisphere, the model shows too large an amplitude between 5°N and 10°N. These characteristics are typical to linear models. This pattern is mainly related to seasonal variability, and it is not observed with such a large amplitude for the interannual sea level anomalies on Figure 4. The large amplitude between 5°N and 10°N is likely to be due to too large a response to the wind stress curl in a region of horizontal shear not properly simulated by the model. Overall the correlation to T/P data (Fig. 3c) is good and is equal to 0.88 in the 5°N-5°S band and 0.82 in the 10°N-10°S band. Similar values are found when

comparing interannual sea level anomalies (Fig. 4). Correlation values larger than 0.85 are found every where in the equatorial band west of 110°W. It is not clear whether the lower correlations near the eastern boundary can be related to the model skill or to the wind forcing as most of the previous features (except the large variability at 5°N near 150°W) are also found when using a more complex model with the same wind forcing (Menkes et al., 1998). The mean rms difference (Fig. 3d) is 4.1cm in the 5°N-5°S band with larger amplitudes in the eastern Pacific. As a conclusion, the model shows a good skill in simulating sea level variability in the equatorial wave guide.

Comparison to TAO zonal current data Comparisons of simulated surface currents to TAO surface data are presented in Figure 5, and statistics are summarized in Table 3. In each plot, the geostrophic zonal current anomalies derived from T/P sea-level anomaly data (anomalies are relative to the 1993-1996 mean) were added to a mean computed from the TAO current data at each location. At 156°E, the model zonal current is correlated at 0.86 to TAO data while T/P comparison to TAO is 0.78. Unfortunately the time series is short and covers only the 1993-1994 period. Interestingly the model and T/P geostrophic currents are correlated at 0.83 over the entire period. This result suggests the model has a good skill in simulating the geostrophic current variability in the western Pacific. Although the model simulates larger amplitudes than TAO or T/P currents at 156°E, these amplitudes remain reasonable especially when considering that a similar result was found by Menkes et al. (1998) in a comparison of an OGCM forced by the same wind data to TAO currents at 156°E. At 165°E, the comparison is similar (0.90), and the T/P zonal current correlates at 0.91 with the TAO data, and correlates at 0.88 with the model zonal currents over the entire period. Eastward, at 140°W and at 110°W, the comparison between the model and TAO currents is weaker (respectively 0.71 and 0.57) while T/P and TAO current

data show correlations equal to 0.70 at 140°W and 0.43 at 110°W. Similarly, the correlations between the model and T/P geostrophic currents are 0.78 at 140°W and 0.49 at 110°W. The result at 110°W is coherent with the one found by Lagerloef et al. (1999). It may be related to the coarse resolution of the T/P data (1° in latitude) which would not properly allow to represent the fine meridional structure of the equatorial current at 110°W when the Equatorial Under Current shallows. To conclude, not only does the model show good correlations to TAO and T/P data, but it also reproduces fairly well the zonal current amplitude. It is worth noting that the model-data good comparisons both for sea level and surface currents give confidence in using the model to understand the role of surface currents on interannual time scale variability in the tropical Paciific Ocean.

Model variability. Figure 6 displays the mean U, V, H and W fields as well as the variability of the seasonal cycle (computed over the 1993-1996 period) and interannual variability (January 1993-December 1998) for each of these fields.

Zonal current. The mean zonal current field displays the two branches of the South Equatorial Current with maximum amplitudes reaching 60cm/s near 2°N. This value is in agreement with climatologies (Reverdin et al., 1994). The model has a lower amplitude along the equator in the eastern Pacific due to the simulation of surface zonal current reversal (Fig. 6a) observed seasonally in spring (Halpern, 1987; McPhaden and Hayes, 1990; McPhaden et al., 1991). Further north, the model does not simulate properly the amplitude of the North Equatorial Counter Current. This may be either due to too strong a friction or to the lack of non-linear processes which would act in strengthening the amplitude of the NECC. The seasonal variability of the zonal currents is mainly located in the central and eastern Pacific (from 160°E to 110°W)

along the equator. This feature is characteristic of the large contribution of the first-mode Rossby wave (Lukas and Firing, 1985) to the seasonal variability in the equatorial Pacific. Indeed, the Rossby wave signatures are clearly observed in Figure 7a where a downwelling Rossby wave (westward currents) is wind-forced in December-January near 140°W and propagates westward. Later, during the boreal spring, an upwelling Rossby wave is wind-forced west of 110°W simultaneously with the weakening of the Trades. Finally, in boreal summer, a weak downwelling Rossby wave is forced near 110°W. Most of these features have also been observed in T/P data and described by Boulanger and Fu (1996). The interannual variability is characterized by a large amplitude at the equator near the dateline extending eastward north of the equator along 1°N-2°N. These two patterns were also observed by Delcroix et al. (1994) in GEOSAT geostrophic zonal currents and are respectively connected to: 1) the location of the equatorial interannual wind variability near the dateline; 2) the meridional displacement of the ITCZ on interannual time scale forcing an asymmetric response in the Ocean.

Meridional current. The mean meridional currents are characterized by the equatorial divergence over most of the basin and amplitudes reaching 4 to 5 cm/s off the equator in agreement with surface drifter measurements (Reverdin et al., 1991). Along the eastern boundary, meridional currents are northward south of 2°N and southward north of that latitude. This pattern results in a convergence of meridional currents around 2°N near the eastern boundary. The variability of meridional currents along the equator is weak (on the order of 1cm/s), but it can strongly impact the meridional location of the equatorial divergence i.e. the location of the maximum of the vertical velocity. On interannual time scales, the variability of the meridional currents is also weak (on the order of 2cm/s). It is worth noting here that the model does reproduce tropical instability waves which have a large meridional component near the equator and which can play

an important role on the sea surface temperature balance (Wand and McPhaden, 1999a,b; Yu and McPhaden, 1999).

Sea level. The mean topography of the simulated sea level displays the major observed features. The sea level is higher in the west than in the east with a difference reaching 50cm. North of the equator, the sea level rises reaching a maximum south of 5°N and then decreases. These features are in agreement with the mean zonal surface currents previously described which are mainly dominated by geostrophic currents. The seasonal variability displays a large amplitude near 5°N. Although the location of this seasonal variability has been observed in data (Kessler, 1990), the model overestimates the sea level response as already observed on Figure 3b. On an interannual time scale, the model reproduces the observed patterns characterized by a large amplitude along the equator in the eastern Pacific and off the equator in the western Pacific (see also Fig. 4b).

Vertical current. The mean vertical current displays an upwelling along the equator in the central Pacific displaced slightly southward in the eastern Pacific. The maximum amplitude reaches 2m/day along the equator between 110°W and 160°W (Fig. 7d) which is similar to the value found in an OGCM forced by the same winds (C. Menkes, personal communication. Further east, the signal decreases as the maximum upwelling amplitude is actually displaced southward (Fig. 5). Further west, the equatorial upwelling also decreases until 142°E where the model coastlines get close to the equator. From 2°N-150°W to south of the equator at the eastern boundary, the model simulates downwelling currents. The major features of seasonal variability (Fig. 6c) are strongly related to the wind seasonal cycle as patterns seems to propagate westward. The variability simulated by the model on seasonal and interannual time scales is rather weak and noisy although one can identifiy a larger variability near the dateline on interannual time scales.

V. Model sensitivity

Various sensitivity experiments have been conducted to determine the set of parameters chosen for the control simulation. The major parameters of the oceanic model are: (1) the baroclinic phase speed (computed from the density gradient and the layer thicknesses), (2) the layer thicknesses, (3) the vertical mixing coefficient (K_u), (4) the number of baroclinic modes and (5) the friction applied to the layer equations. Considering that most of the model sensitivity studies are straightforward or do not show significant differences of the major patterns of variability to the reference simulation, most of the results will be only briefly discussed and only the sensitivity to the friction (point 5) is illustrated:

(1) The model simulations are not very sensitive to the baroclinic phase speed for values typical of the tropical Pacific Ocean (Picaut and Tournier, 1993) i.e. ranging from 2m/s to 3m/s for the first mode and from 1m/s to 1.5m/s for the second baroclinic mode. Thus the model comparisons to data are similar to the ones presented previously and are not illustrated.

(2) Schematically near the equator, the shear-layer surface currents are proportional to the coefficient $H_2 \big/ \big(K_u (H_1 + H_2) \big)$ while the baroclinic solution depends on $1 \big/ (H_1 + H_2)$ for the momentum equations and $(H_1 H_2) \big/ \big(K_u (H_1 + H_2) \big)$ for the thickness layer equation (same dependence for the shear-layer vertical velocity). Thus, if H_1 decreases (increases), the shear-layer currents strengthen (weaken and converge toward zero) while the vertical velocity converges toward zero (a constant value function of $1/K_u$), and the baroclinic solution strengthens and depends on the value of H_2 (weakens). If H_2 decreases (increases), the shear-layer solution weakens (strengthens but converges toward a constant solution), but the baroclinic solution strengthens (weakens). To conclude, the sea level and zonal surface current (mainly due to the baroclinic currents) solutions strengthen (weaken) when any of the layer thicknesses decreases

(increases) while the shear-layer solution has a different behavior depending on which thickness layer is changed. Finally, as the first layer depth is taken constant to 50m to compare with other similar models, a change in H_2 would either intensify or decrease the sea level and current amplitudes degrading the model comparison to data without modifying the major patterns. It is therefore not worth being illustrated.

(3) As introduced above, near the equator, the shear-layer solution (horizontal and vertical currents) is proportional to the value of $1/K_u$ while the baroclinic solution mainly depends on $1/K_u$ through the flux of mass between the two layers. When a linear Rayleigh friction is used, the baroclinic solution is strongly degraded when K_u decreases, while it is weakly affected when it increases from the value chosen in the control run. When the model is run with a quadratic friction, the baroclinic current solution cannot reach very a large amplitude. Thus the sensitivity to K_u is weaker although the solution is slightly degraded for small values. Therefore the main sensitivity to K_u is through the shear surface currents and the vertical velocity at the equator. The value of K_u in the control run has been chosen by comparison to the mean upwelling velocity along the equator in the OPA ocean general circulation model (using a 1.5 closure Turbulent Kinetic Energy scheme, Blanke and Delecluse, 1993) forced by the same wind forcing (on the order of 2m/day; C. Menkes, personal communication). As a final comment, the reference value of K_u is 6.5×10^{-5} $m^2.s^{-1}$ and the time scale associated to the transfer of momentum from the surface layer to the subsurface layer $(K_u(H_1+H_2)/H_1H_2)^{-1}$ is equal to 2.97days. As a comparison, the mixed-layer damping time is taken to be 2 days in Zebiak and Cane (1987) and in Battisti (1988), and is increased to 3 days in Chen et al. (1995).

(4) It is often argued that simple models simulate better the surface zonal currents when more than one baroclinic mode is considered (Chen et al., 1995; Dewitte, 1999). Thus, the model

has been run with one subsurface layer only which thickness is taken equal to the first subsurface layer thickness in the control run (see Table 1 for the simulation parameters). Only the first layer density has been changed for the model phase speed not to be too small. As can be seen in Table 2, the model comparison to T/P data is only slightly degraded. Similarly, the model comparison to TAO currents is weaker in the equatorial Pacific (Table 3). However the model major patterns (not shown here) are similar to the ones shown in Figures 3, 4, 5 and 6. To conclude, it appears that considering two baroclinic modes to represent the equatorial dynamics only slightly performs better than considering one single baroclinic mode. This result is different from the one found in linear models using a linear Rayleigh friction. Indeed, in such models, the model-data comparison is significantly affected by the use of higher baroclinic modes which main effect is to reduce the actual amplitude of Rossby waves propagating toward the western Pacific Ocean and therefore to weaken the unrealistic amplitudes of the surface currents simulated with one baroclinic mode only.

(5) A crucial parameter for the baroclinic solution is the intensity and formulation of the friction. Two simulations are discussed in the following in order to evaluate the actual improvement brought by choosing a quadratic friction on the momentum equations,. The first sensitivity simulation (Exp. CBS) is performed using similar values to the control run presented by Chen et al. (1995). It will be used to discuss the impact of weak Rayleigh friction values (Zebiak and Cane, 1987; Battisti, 1988; Picaut et al., 1997; Dewitte, 1999) as well as the improvement brought to the simulation of surface currents when more than one baroclinic mode is considered in the context of using a weak Rayleigh friction. The second one (Exp. R6m) is performed using a constant $(6 \text{months})^{-1}$ linear Rayleigh friction in the momentum and thickness layer equations. This value has been suggested to give a better comparison to observations than

weaker values currently used (Picaut et al., 1993). In comparison to the control run simulation and in order to present the best possible comparison to data, the layer thicknesses have been increased while the ratio of mode 1 vs. mode 2 has been kept constant, and as a consequence the K_u value has been increased to keep the equatorial vertical velocity amplitude similar to the control run (see Table 1 for the simulation parameters). Thus, the model retains a sea level pattern with amplitude comparable to T/P data.

Exp. CBS. The model was run with parameters (see Table 1) similar to those chosen by Chen et al. (1995). These values are in the range to most of the studies using linear models (Zebiak and Cane, 1987; Picaut et al., 1997; Dewitte, 1999) whether these models include one or more baroclinic modes. Not only the comparisons to T/P data are deteriorated (0.72 on average over 5°N-5°S, seeTable 2), but also the comparisons to TAO current data are much weaker at all locations (Table 3). Interestingly and as previously stated, Figure 8 shows that the variability at 110°W reproduces the seasonal reversal of the currents. However, westward, the model mean state is far from the observations and the variability is poorly simulated. These results are confirmed in the spatial patterns of the mean state, and seasonal and interannual variability of each field (Fig. 9). Various points are worth noting: 1- the mean zonal currents are unrealistic both at the equator and off the equator; 2- the seasonal and interannual zonal current variability are much larger in the western Pacific and off the equator in the central Pacific than in the control experiment or in observations (Delcroix et al., 1995; Picaut and Delcroix, 1996). It is worth noting that similar features are actually observed in the seasonal cycle provided with the Zebiak and Cane model which is currently used for seasonal forecast; 3- the meridional current patterns are not significantly affected although the variability is slightly stronger; 4- the mean sea level is changed as the zero line is displaced eastward although the mean difference between the east and

west boundaries are similar; 5- the seasonal and interannual sea level patterns display larger amplitudes than in the control run especially off the equator and in the western Pacific, but except for the larger amplitude of the sea level and the inability of the model to properly reproduce the amplitude ratio between the western Pacific and the eastern Pacific, the major patterns are similar to those currently observed.

Exp. R6m. The comparison to T/P sea level data (Table 2) is worse (0.81 as a mean correlation over 5°N-5°S) and the model shows a much larger variability especially in the western Pacific (not shown). This larger variability can be observed on the equatorial zonal currents (Fig. 10) especially west of 110°W i.e. along the propagation of the Rossby waves. The use of a strong friction (6 months) in the baroclinic equations is not sufficient to damp properly the Rossby wave amplitudes on both seasonal and interannual time scales. Hence the model comparison to TAO zonal currents is worse at all locations (except 156°E) and the model variability is much larger than in the control run. These features can be also observed in Figure 11. Various points are worth noting: 1- the mean zonal surface currents reach large unrealistic amplitudes (above 80cm/s at 2°N) compared to observed climatologies (Reverdin et al., 1994) and the zonal current patterns on seasonal and interannual time scales show larger variability although the general patterns are mostly similar to the control run; 2- the meridional currents and mean vertical currents are not significantly altered; 3- the seasonal and interannual sea level patterns show significantly larger amplitudes in the off-equatorial latitudes and in the western Pacific although the equatorial variability in the eastern Pacific is smaller than in the control run and in the observations. Therefore the use of a same Rayleigh friction in the baroclinic equations has the consequence of overestimating the Rossby wave amplitudes, and if the Rayleigh friction is too strong, to underestimate the Kelvin wave amplitude in the eastern Pacific. When using one baroclinic mode

only (not shown here), all the energy goes in the first mode. Therefore, more energy reaches the western Pacific and the comparison with T/P sea level and TAO currents is worse. Also, in this linear ocean model, the reversal of the zonal currents in boreal spring is due to the seasonal upwelling Rossby wave (westward currents). This can be produced by a model with one baroclinic mode only. However when the model is run with more baroclinic modes and that a strong friction (stronger than 6 months) is applied on the additional baroclinic modes, the upwelling Rossby waves will be damped too fast and the model will neither properly reproduce the mean equatorial minimum of the zonal currents, nor the reversal of the currents in spring. In such a case, a weaker Rayleigh friction would be required, but the model would then overestimate the Rossby wave amplitudes in the west.

We conlude from these results that, in linear models, a quadratic friction in the momentum equations is required to properly reproduce both the eastern and western Pacific variability, and to simulate both the sea level and surface current mean patterns and variability on seasonal and interannual time scales.

VI. Discussion and conclusions
The aim of the present work is to bring a quantitative estimate of the role of long equatorial waves and their reflection during the strong 1997-1998 ENSO period. A preliminary step has been to develop a model of the equatorial Pacific basin, which could be used as a reliable tool to understand the role of long equatorial waves. This simple ocean model, named Trident, is composed of a dynamical and a themodynamical component. In this first paper, only the ocean dynamics are described. Briefly, the ocean dynamics is derived from a linear 3-1/2 layer model with a constant surface layer (mixed-layer). Fluxes of mass and momentum are allowed between

the first and second layers. That set the forcing conditions for the subsurface dynamics. As the

surface layer has a constant depth, two baroclinic modes exist in the model. Although Chen et al.

(1995) showed that the introduction of a second baroclinic mode helped in improving the model

representation of surface currents, the present model with one baroclinic mode shows similar skill

(only slightly weaker) in representing the sea level variability (T/P sea level data) and equatorial

surface currents (TAO surface currents at 10m). It is worth noting that this results is mainly due

to the introduction of a quadratic friction in the momentum equation. The model performs well in

simulating surface and vertical currents and sea level mean patterns as well as their seasonal and

interannual variability.

A study of the model sensitivity to various parameters clearly highlight that: 1-a linear

ocean model is unlikely to represent the equatorial surface current amplitudes as well as the sea

level amplitude ratio between the western and eastern Pacific when a Rayleigh friction is applied

to the baroclinic equations; 2- the use of large Rayleigh friction as it has been done in most of the

linear models whether one or more baroclinic modes are considered (Zebiak and Cane, 1987;

Battisti, 1988; Chen et al., 1995; Picaut et al., 1997; Dewitte, 1999) deteriorates the model skill in

simulating surface currents potentially important for ENSO. However, in each sensitivity

experiment, we did not find the sea level patterns to be significantly altered. This point clearly

raises the question of whether sea level data are sufficient to validate models. Dramatic changes

in the model parameters and therefore in the potential mechanisms at work in the model for the

ocean and for ENSO lead to very similar sea level patterns but large changes in the surface zonal

current fields. Considering that thermocline displacements are important in the east, but that

zonal advection is important in the central Pacific (Picaut et al., 1996), it is crucial in order to

study the importance of the different oceanic mechanisms at work at ENSO time scales to use a model which performs well in simulating both the sea level and the surface currents.

In a companion paper, the thermodynamical model is presented and evaluated with respect to observations. Moreover, the impacts of long equatorial wave reflection (especially during the 1997-1998 El Niño/La Niña period) at both the eastern and western boundaries are investigated in terms of sea level, surface currents and sea surface temperature anomalies.

APPENDIX A

The scheme used to solve the linear shallow-water equations in the long-wave approximation is similar to the one described by Cane and Patton (1984) and used in the Zebiak and Cane (1987) model. First, the equations are non-dimensionalized: c, the mode phase speed, is a scale for the currents, c^2/g is a scale for the layer thickness, $T=(c\beta)^{-1/2}$ is the time scale, $L=(c/\beta)^{1/2}$ is the length scale, while F and G, the zonal and meridional forcing terms, are non-dimensionalized by $c(c\beta)^{1/2}$, and Q, by $(c^2(c\beta)^{1/2})/g$. Then the Kelvin wave and long Rossby wave solutions are solved separately.

Kelvin wave solution. The Kelvin wave coefficient verifies

$$\left(\partial_t + \partial_x\right)a_K = b_K = \int_{Y_S}^{Y_N} (F+Q)\Psi_K dy \bigg/ \left(2\int_{Y_S}^{Y_N} \Psi_K^2 dy\right)$$

The scheme used in the model is different from the one described by Cane and Patton (1984) where the Kelvin coefficient is computed along its wave characteritics. The equation is integrated from west to east, the initial condition at the western boundary being determined by the long Rossby wave reflection:

$$a_{i+1}^{n+1} = 2\Delta t b_i^n + a_i^{n-1} + (1-\alpha)/(1+\alpha)\left[a_{i+1}^{n-1} - a_i^{n+1}\right]$$

where $\alpha = \Delta t/\Delta x$.

Non-Kelvin wave solution. The non-Kelvin wave solution is composed of the long Rossby and the anti-Kelvin waves, both propagating westward. The equations are:

$$\left\{ \begin{array}{l} \dfrac{1}{4\Delta t}\left(u_{i+1,j}^{n+1} + u_{i,j}^{n+1} - u_{i+1,j}^{n-1} - u_{i,j}^{n-1}\right) - \dfrac{1}{4}\,y_j^u\left(v_{i,j+1}^{n+1} + v_{i,j}^{n+1} + v_{i,j+1}^{n-1} + v_{i,j}^{n-1}\right) \\[2ex] \qquad\qquad\qquad + \dfrac{1}{2\Delta x}\left(h_{i+1,j}^{n+1} - h_{i,j}^{n+1} + h_{i+1,j}^{n-1} - h_{i,j}^{n-1}\right) = \tilde{F}_{i,j}^{n} \\[2ex] \qquad\qquad\qquad + \dfrac{1}{4}\,y_j^u\left(u_{i,j}^{n+1} + u_{i,j}^{n-1}\right) + \dfrac{1}{4}\,y_{j-1}^u\left(u_{i,j-1}^{n+1} + u_{i,j-1}^{n-1}\right) \\[2ex] \qquad\qquad\qquad + \dfrac{1}{2\Delta y}\left(h_{i,j}^{n+1} - h_{i,j-1}^{n+1} + h_{i,j}^{n-1} - h_{i,j-1}^{n-1}\right) = \tilde{G}_{i,j}^{n} \\[2ex] \dfrac{1}{4\Delta t}\left(h_{i+1,j}^{n+1} + h_{i,j}^{n+1} - h_{i+1,j}^{n-1} - h_{i,j}^{n-1}\right) + \dfrac{1}{2\Delta x}\left(u_{i+1,j}^{n+1} - u_{i,j}^{n+1} + u_{i+1,j}^{n-1} - u_{i,j}^{n-1}\right) \\[2ex] \qquad\qquad\qquad + \dfrac{1}{2\Delta y}\left(v_{i,j+1}^{n+1} - v_{i,j}^{n+1} + v_{i,j+1}^{n-1} - v_{i,j}^{n-1}\right) = \tilde{Q}_{i,j}^{n} \end{array} \right.$$

Introducing

$$\left\{ \begin{array}{l} S_{i,j}^{u} = \tilde{F}_{i,j}^{n} + \dfrac{1}{4}\,y_j^u\left(v_{i,j+1}^{n-1} + v_{i,j}^{n-1}\right) - \dfrac{1}{4\Delta t}\left(u_{i+1,j}^{n+1} - u_{i+1,j}^{n-1} - u_{i,j}^{n-1}\right) - \dfrac{1}{2\Delta x}\left(h_{i+1,j}^{n+1} + h_{i+1,j}^{n-1} - h_{i,j}^{n-1}\right) \\[2ex] S_{i,j}^{v} = \tilde{G}_{i,j}^{n} - \dfrac{1}{4}\left(y_j^u u_{i,j}^{n-1} + y_{j-1}^u u_{i,j-1}^{n-1}\right) - \dfrac{1}{2\Delta y}\left(h_{i,j}^{n-1} - h_{i,j-1}^{n-1}\right) \\[2ex] S_{i,j}^{h} = \tilde{Q}_{i,j}^{n} - \dfrac{1}{2\Delta y}\left(v_{i,j+1}^{n-1} - v_{i,j}^{n-1}\right) - \dfrac{1}{4\Delta t}\left(h_{i+1,j}^{n+1} - h_{i+1,j}^{n-1} - h_{i,j}^{n-1}\right) - \dfrac{1}{2\Delta x}\left(u_{i+1,j}^{n+1} + u_{i+1,j}^{n-1} - u_{i,j}^{n-1}\right) \end{array} \right.$$

the system can be rewritten

$$\left\{ \begin{array}{l} \qquad\qquad \dfrac{1}{4\Delta t}\left(u_{i,j}^{n+1}\right) - \dfrac{1}{2\Delta x}\left(h_{i,j}^{n+1}\right) = S_{i,j}^{u} + \dfrac{1}{4}\,y_j^u\left(v_{i,j+1}^{n+1} + v_{i,j}^{n+1}\right) \\[2ex] \dfrac{1}{4}\left(y_j^u u_{i,j}^{n+1} + y_{j-1}^u u_{i,j-1}^{n+1}\right) + \dfrac{1}{2\Delta y}\left(h_{i,j}^{n+1} - h_{i,j-1}^{n+1}\right) = S_{i,j}^{v} \\[2ex] \qquad\qquad \dfrac{1}{4\Delta t}\left(h_{i,j}^{n+1}\right) - \dfrac{1}{2\Delta x}\left(u_{i,j}^{n+1}\right) = S_{i,j}^{h} - \dfrac{1}{2\Delta y}\left(v_{i,j+1}^{n+1} - v_{i,j}^{n+1}\right) \end{array} \right.$$

Then introducing similar notation as in Cane and Patton (1984):

$$\left\{ \begin{array}{l} R_{i,j}^{u} = S_{i,j}^{u} + 2\alpha S_{i,j}^{h} \\[1ex] R_{i,j}^{h} = S_{i,j}^{h} + 2\alpha S_{i,j}^{u} \end{array} \right.$$

u and h can be expressed as functions of v

$$\left[\begin{array}{l} u_{i,j}^{n+1} = \dfrac{4\Delta t}{\left(1-4\alpha^2\right)} \left\{ R_{i,j}^u + v_{i,j+1}^{n+1}\left(\dfrac{1}{4}y_j^u - \dfrac{\alpha}{\Delta y}\right) + v_{i,j}^{n+1}\left(\dfrac{1}{4}y_j^u + \dfrac{\alpha}{\Delta y}\right) \right\} \\[6pt] h_{i,j}^{n+1} = \dfrac{4\Delta t}{\left(1-4\alpha^2\right)} \left\{ R_{i,j}^h + v_{i,j+1}^{n+1}\left(\dfrac{\alpha}{2}y_j^u - \dfrac{1}{2\Delta y}\right) + v_{i,j}^{n+1}\left(\dfrac{\alpha}{2}y_j^u + \dfrac{1}{2\Delta y}\right) \right\} \end{array}\right.$$

where v is solution of the second order equation

$$v_{i,j+1}^{n+1}\left(\left(y_j^u\right)^2\Big/4 - 1\Big/(\Delta y)^2\right) + v_{i,j}^{n+1}\left(\left(\left(y_j^u\right)^2 + \left(y_{j-1}^u\right)^2\right)\Big/4 + 2\Big/(\Delta y)^2 + 2\alpha\right) + v_{i,j-1}^{n+1}\left(\left(y_{j-1}^u\right)^2\Big/4 - 1\Big/(\Delta y)^2\right)$$

$$= \left[\left(1-4\alpha^2\right)\Big/\Delta t\right]S_{i,j}^v - \left(y_j^u R_{i,j}^u + y_{j-1}^u R_{i,j-1}^u\right) - 2\left(R_{i,j}^h - R_{i,j-1}^h\right)\Big/\Delta y$$

Partial boundary conditions. The method to compute the influence of partial boundaries onto the Kelvin and Rossby (+anti-Kelvin) waves is the same as the one described by duPenhoat et al. (1983) and used by Cane and Patton (1984). The reader is thus referred to these two articles for details.

Acknowledgements

REFERENCES

Arakawa, A., Computational design for long term numerical integration of the equations of fluid motion, two dimensional incompressible flow, Part. I, *J. Comput. Phys.*, I, 119-149, 1966.

Battisti D. S., Dynamics and thermodynamics of a warming event in a coupled tropical atmosphere-ocean model, *J. Atmos. Sc.*, **45**, 2889-2819, 1988.

Bentamy, A., Y. Quilfen, F. Gohin, N. Grima, M. Lenaour, and J. Servain, Determination and validation of average wind fields from ERS-1 scatterometer measurements, *The Global Atmopshere and Ocean System*, **4**, 1-29, 1996.

Boulanger, J.-P, and L.-L. Fu, Evidence of boundary reflection of Kelvin wave and first-mode Rossby waves from TOPEX/POSEIDON sea level data, *J. Geophys. Res.*, **101**, 16361-16371, 1996.

Boulanger, J.-P, and C. Menkes, Long equatorial wave reflection in the Pacific Ocean from TOPEX/POSEIDON during the 1992-1998 period, *Clim. Dyn.*, 1999, in press.

Boulanger, J.-P, and C. Menkes, Propagation and reflection of long equatorial waves in the Pacific ocean during the 1992-1993 El Niño, *J. Geophys. Res.*, **100**, 25041-25059, 1995.

Cane, M. A., and R. J. Patton, A numerical model for low-frequency equatorial dynamics, *J. Phys. Oceanogr.*, **12**, 1853-1863, 1984.

Chen, D., L. M. Rothstein, and A. J. Busalacchi, A hybrid vertical mixing scheme and its application to tropical ocean models, *J. Phys. Oceanogr.*, **24**, 2156-2179, 1994.

Chen, Y.-Q., D. S. Battisti, and E. S. Sarachik, A new ocean model for studying the tropical oceanic aspects of ENSO, *J. Phys. Oceanogr.*, **25**, 2065-2089, 1995.

Delcroix, T., J.-P. Boulanger, F. Masia, and C. Menkes, GEOSAT-derived sea level and surface-current anomalies in the equatorial Pacific, during the 1986-1989 El Niño and La Niña, *J. Geophys. Res.*, **99**, 25093-25107, 1994.

Dewitte, B., Sensitivity of an intermediate ocean-atmosphere coupled model of the Tropical Pacific to its oceanic structure, *J. Clim.*, submitted, 1999.

DuPenhoat, Y., M. A. Cane,. and R. J. Patton, Reflections of low-frequency equatorial waves on partial boundaries, *Hydrodynamics of the equatorial oceans*, J. C. J. Nihoul, Ed., Elsevier, 237-258, 1983.

Halpern, D., Observations of annual and El Niño thermal and flow variations at 0°, 110°W and 0°, 95°W during 1980-1985, *J. Geophys. Res.*, **92**, 7289-7312, 1987.

Hayes, S. P., L. J. Mangum, J. Picaut, A. Sumi, and K. Takeuchi: TOGA-TAO: A moored array for real-time measurements in the tropical Pacific ocean, *Bull. Am. Met. Soc.*, **72**, 3,339-347.

Kessler, W. S., and M. J. McPhaden, Oceanic equatorial waves and the 1991-1993 El Niño, *J. Climate*, **8**, 1757-1774, 1995.

Kessler, W. S., and J. P. McCreary, The annual wind-driven Rossby wave in the subthermocline equatorial Pacific, *J. Phys. Oceanogr.*, **23**, 1192-1207, 1993.

Lee, T., J.-P. Boulanger, L.-L. Fu, A. Foo, and R. Giering, Couple data assimilation and ENSO prediction: an application to the 97-98 El Niño, in preparation.

Mantua, N. J. and D. S. Battisti, Evidence for the delayed oscillator mechanism for ENSO: The "observed" oceanic Kelvin mode in the far western Pacific, *J. Phys. Oceanogr.*, **24**, 691-699, 1994.

McPhaden M. J., TOGA-TAO and the 1991-93 El Niño-Southern Oscillation event, *Oceanography*, **6**, 36-44, 1993.

McPhaden, M. J., and M. E. McCarthy, Mean seasonal cycles and interannual variations at 0°,110°W and 0°,140°W during 1980-1991, NOAA technical Memorandum ERL PMEL-95, 118pp, 1992.

Mc Phaden, M. J., D. V. Hansen, and P. L. Richardson, A comparison of ship drift, drifting buoy, and current meter mooring velocities in the Pacific South Equatorial Current, *J. Geophys. Res.*, **96**, 775-781, 1991.

McPhaden M. J., and S. P. Hayes, Moored velocity, temperature and wind measurements in the equatorial Pacific Ocean: a review of scientific results, 1985-1990*. Intl. TOGA Scientific Conf. Proc.*, Geneva, Switzerland, World Meteorological Organization, 59-69, 1990.

Menkes, C., J.-P. Boulanger, A.J. Busalacchi, J. Vialard, P. Delecluse, M.J. McPhaden, E. Hackert, and N. Grima, Impact of TAO vs. ERS wind stresses onto simulations of the tropical Pacific Ocean during the 1993-1998 period by the OPA OGCM, *Climatic Impact of Scale Interactions for the Tropical Ocean-Atmosphere System*, pp. 46-48, Euroclivar Workshop Report, Eucliv 13, December 1998.

Menkes, C., J.-P. Boulanger, and A. J. Busalacchi, Evaluation of TOPEX and basin-wide Tropical Ocean Global Atmosphere-Tropical Atmosphere Ocean sea surface topographies and derived geostrophic currents, *J. Geophys. Res.*, **100**, 25087-25099, 1995.

Picaut, J., F. Masia, and Y. duPenhoat, An advective-reflective conceptual model for the oscillatory nature of the ENSO, *Science*, **277**, 663-666, 1997.

Picaut, J., M. Ioualalen, C. Menkes, T. Delcroix, and M. J. McPhaden, Mechanism of the zonal displacements of the Pacific warm pool: implications for ENSO, *Science*, **274**, 1486-1489, 1996.

Picaut, J., and T. Delcroix, Equatorial wave sequence associated with warm pool displacements during the 1986-1989 El Niño-La Niña, *J. Geophys. Res.*, **100**, 18393-18408, 1995.

Picaut, J., C. Menkes, J.-P. Boulanger, and Y. duPenhoat, Dissipation in a Pacific equatorial long wave model, TOGA-*Notes*, 10, Nova Univ. Press, Dania, FL, 11-15, 1993.

Reverdin G., Frankignoul C., Kastenare E., and M. J. McPhaden, Seasonal variability in the surface currents of the equatorial Pacific, *J. Geophys. Res.*, 20323-20344, 1994

Schopf, P. S., and M. J. Suarez, Vacillations in a coupled ocean-atmosphere model, *J. Atmos. Sci.*, **45,** 549-566, 1988.

Tapley, B. D., D. P. Chambers, C. K. Shum, R. J. Eanes, and J. C. Ries, Accuracy assessment of the large-scale dynamic ocean topography from TOPEX/POSEIDON altimetry, J. Geophys. Res., 99, 24605-24617, 1994.

Wang, W, and M. J. McPhaden, The surface layer heat balance in the equatorial Pacific ocean, Part I: Mean seasonal cycle, *J. Phys. Oceanogr.*, in press.

Wang, W, and M. J. McPhaden, The surface layer heat balance in the equatorial Pacific ocean, Part II: Interannual variability, *J. Phys. Oceanogr.*, accepted.

Yu, X, and M. J. McPhaden, Seasonal variability in the equatorial Pacific, *J. Phys. Oceanogr.*, **29**, 925-947, 1999.

Zebiak, S. E., and M. A. Cane, A model El Niño/Southern Oscillation, *Mon. Wea. Rev.*, **115**, 2262-2278, 1987.

FIGURE CAPTIONS

Figure 1: Model boundaries and domain. Real coastline are superimposed.

Figure 2: Model discretization grid. U, V, W, H, T, F, G and Q respectively refer to the zonal current, meridional current, vertical current, sea level (or pressure), temperature, zonal forcing, meridional forcing and "mass" forcing.

Figure 3a-d: (a) Standard deviation of TOPEX/POSEIDON sea level anomalies (contours are every 1 cm; values higher than 7cm are shaded). (b) Standard deviation of the simulated sea level anomalies (contours are every 1 cm; values higher than 7cm are shaded). (c) Map of correlation between T/P and simulated sea level anomalies (contour intervals are every 0.1 from 0. to 0.8, and every 0.05 from 0.80 to 0.95; values higher than 0.7 are shaded). (d) Map of rms difference between T/P and simulated sea level anomalies (contours are every 1 cm; values higher than 7cm are shaded).

Figure 4a-d: Same as Figure 3 but interannual sea level anomalies are considered (anomalies are computed relative to the 1993-1996 seasonal cycle).

Figure 5a-d: Time series at (a) 156°E, (b) 165°E, (c) 140°W and (d) 110°W of TAO zonal current data (solid line), simulated zonal currents (dashed line) and T/P geostrophic zonal currents (dotted line) with their mean being equal to the TAO mean currents. Statistical comparisons are summarized in Table 3.

Figure 6: Longitude-latitude maps (130°E-80°W/10°S-10°N) of the mean surface zonal current (contour intervals every 10cm/s, negative values are shaded), meridional current (contour intervals every 2cm/s, negative values are shaded), sea level (contour intervals every 10cm, negative values are shaded) and vertical current at 50m (contour intervals every 0.5m/day, negative values are shaded), and of the seasonal and interannual variability of zonal current

(contour intervals every 5cm/s; values higher than 20cm/s are shaded), meridional current (contour intervals every 1cm/s; values higher than 2cm/s are shaded) and sea level (contour intervals every 1cm; values higher than 7cm are shaded).

Figure 7: (a) Longitude-time section plot of the simulated climatological equatorial surface zonal current anomalies (contours are every 15cm/s and negative values are shaded; three years are presented for clarity); (b) Longitude section of the equatorial mean surface zonal current; (c) Longitude-time section plot of the simulated climatological vertical velocity (contours are every 0.5m/day and negative values are shaded; three years are presented for clarity); (d) Longitude section of the equatorial mean vertical velocity.

Figure 8: Same as Figure 5, but the model is run with parameters similar to those used by Chen et al. (1995).

Figure 9: Same as Figure 6, but the model is run with parameters similar to those used by Chen et al. (1995).

Figure 10: Same as Figure 5, but the model is run with a 6-month Rayleigh friction. Parameters are summarized in Table 1, and statistical comparisons are summarized in Table 3.

Figure 11: Same as Figure 6, but the model is run with a 6-month Rayleigh friction.

	Control	Exp. M1	Exp. CBS	Exp. R6m
H_1	50m	50m	50m	50m
H_2	25m	25m	75m	60m
H_3	125m	-	100m	190m
ρ_1	1022kg.m^{-3}	1020kg.m^{-3}	1022kg.m^{-3}	1022kg.m^{-3}
ρ_2	1025.4kg.m^{-3}	1028kg.m^{-3}	1025.4kg.m^{-3}	1025.4kg.m^{-3}
ρ_3	1028kg.m^{-3}	-	1028kg.m^{-3}	1028kg.m^{-3}
c_1	2.5m/s	2.4m/s	2.9m/s	3.0m/s
c_2	1.1m/s	-	1.1m/s	1.3m/s
γ_1	1.6	1	1.22	1.6
γ_2	2.6	-	5.63	2.6
Fric$_1$ (u,v)	1.67*	1.67*	(30 months)$^{-1}$	(6 months)$^{-1}$
Fric$_1$ (h)	(6 months)$^{-1}$	(6 months)$^{-1}$	(30 months)$^{-1}$	(6 months)$^{-1}$
Fric$_2$ (u,v)	3.33*	-	(30 months)$^{-1}$	(6 months)$^{-1}$
Fric$_2$ (h)	(6 months)$^{-1}$	-	(30 months)$^{-1}$	(6 months)$^{-1}$
K_u	$6.5.10^{-5}$	$6.5.10^{-5}$	2.10^{-4}	$1.5.10^{-4}$

Table 1: Model parameters for different sensitivity experiments. *unit is in months^{-1}.m^{-1}.s. H1 is the model surface layer (mixed-layer) thickness, H2 is the thickness of the second layer, H3 is the thickness of the third layer when it applies. ρ_1 is the density in the first subsurface layer, ρ_2 is the density in the deep layer at rest in the experiments Exp M1 (single baroclinic mode), it is the density in the second subsurface layer in the other experiments, ρ_3 is the density in the deep layer at rest in these same experiments. c_1 is the phase speed of the first baroclinic phase speed. c_2 is the phase speed of the second baroclinic phase speed when it applies. γ_1 and γ_2 are the amplitudes of the first and second vertical modes in the first subsurface layer. When only one layer is considered, only the first value exists and is equal to 1. Then the forcing is projected over the depth H1+H2. When two baroclinic modes are considered, these values are used to compute the actual depth onto which the forcing is projected for each mode: it is respectively γ_1(H1+H2) and γ_2(H1+H2) for the first and second baroclinic modes. These values are respectively 121m and 197m in the control run, 152m and 703m in Exp.CBS, 176m and 286m in Exp. R6m i.e. showing that the amplitude of the second baroclinic mode is relatively weak in Exp.CBS. Fric$_{1,2}$ (u,v) is the friction coefficient applied to the momentum equations respectively for the first and second subsurface layers when it applies. The friction is quadratic in the control experiment, it is a linear Rayleigh friction in the others. Fric$_{1,2}$ (h) is the linear Rayleigh friction coefficient applied to the thickness layer equation respectively for the first and second subsurface layers when it applies. K_u measures a coefficient of vertival transfer of momentum between the surface layer and the first subsurface layer.

	Control	ExpM1	ExpCBS	ExpR6m
5°N-5°S	0.88	0.88	0.72	0.81
	8.6	9.0	10.9	9.1
	4.1	4.3	7.8	5.6

Table 2: Model comparisons to TOPEX/POSEIDON sea level data for different experiments. The mean rms of T/P data is 7.7cm in 5°N-5°S. The first number is the correlation, the second one is the model rms (in cm), the third one is the rms difference (in cm).

	156°E 22.0cm/s	165°E 35.1cm/s	140°W 32.7cm/s	110°W 33.5cm/s
T/P	0.77 16.6 13.9	0.91 23.4 16.9	0.69 24.7 23.7	0.43 22.0 31.3
Control	0.86 30.4 15.9	0.90 38.5 16.8	0.71 35.5 26.3	0.57 24.2 27.9
Exp. M1	0.87 30.9 16.2	0.88 40.6 19.4	0.68 34.5 26.8	0.58 23.3 27.7
Exp. CBS	0.44 77.5 70.6	0.12 64.2 69.3	0.37 56.4 53.6	0.19 33.3 42.5
Exp. R6m	0.77 36.7 24.1	0.76 45.1 29.6	0.66 41.8 32.0	0.55 27.7 29.3

Table 3: Model comparisons to TAO surface zonal currents for different experiments. The first number is the correlation, the second one is the model rms (in cm/s), the third one is the rms difference (in cm/s). The first line is the comparison between T/P derived geostrophic currents and TAO data.

Figure 1:

G   V   G

j+1

U

W,T,F,Q

U

j

G   V   G
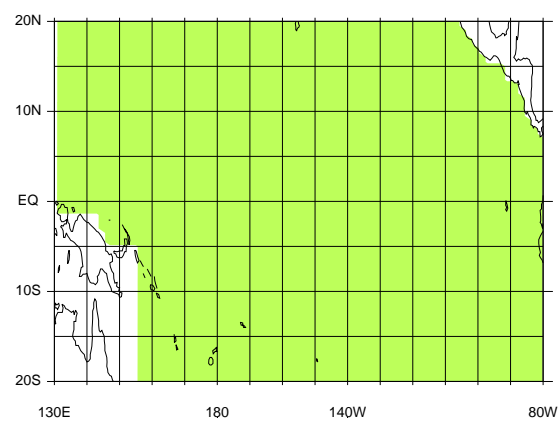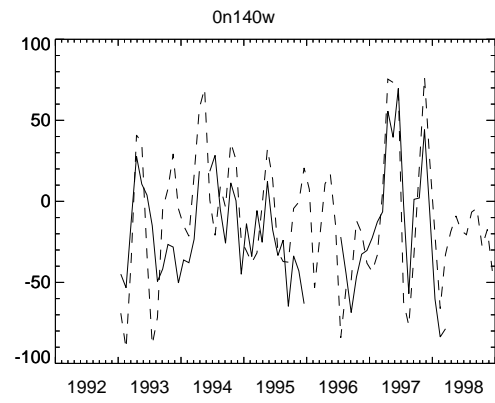
i   i+1
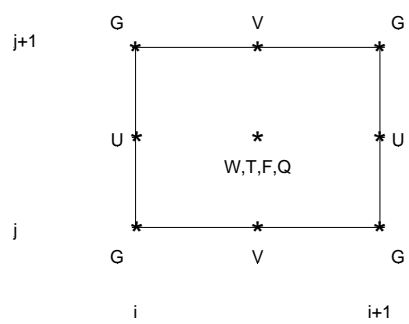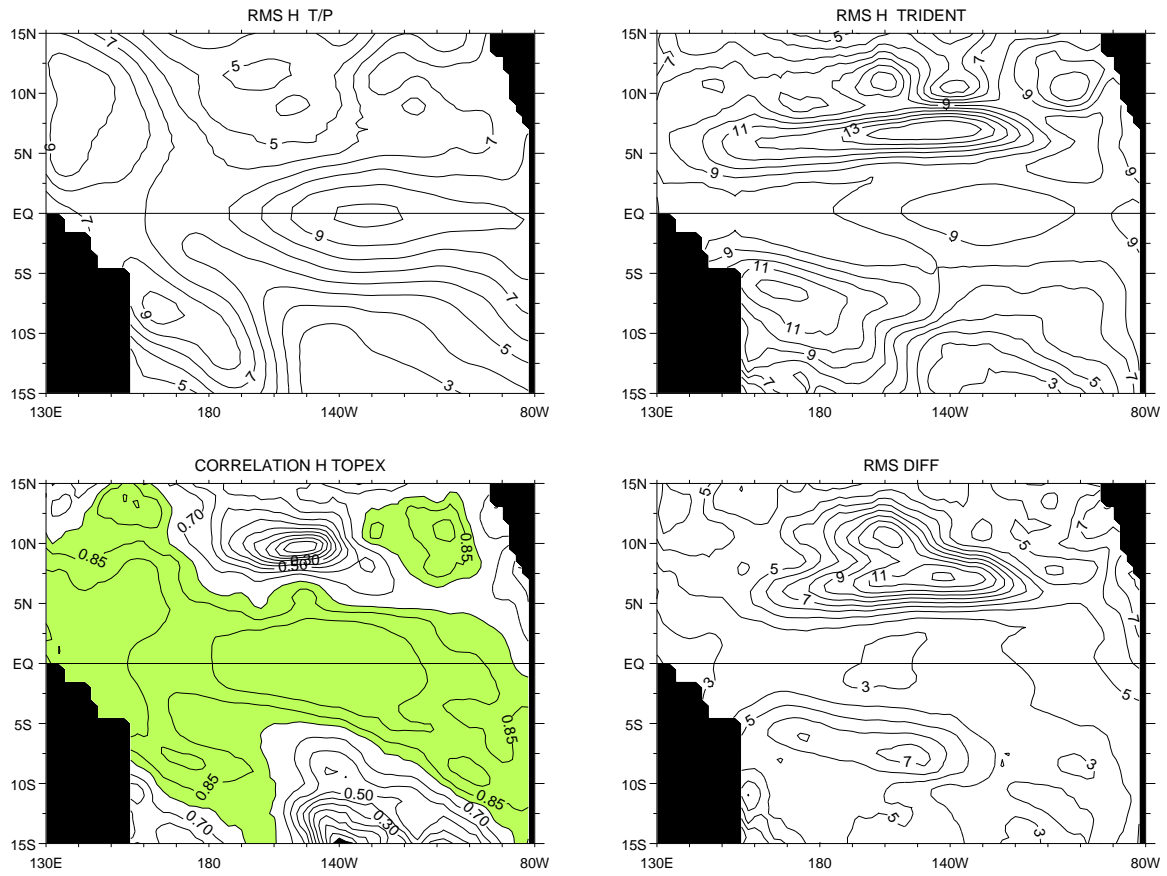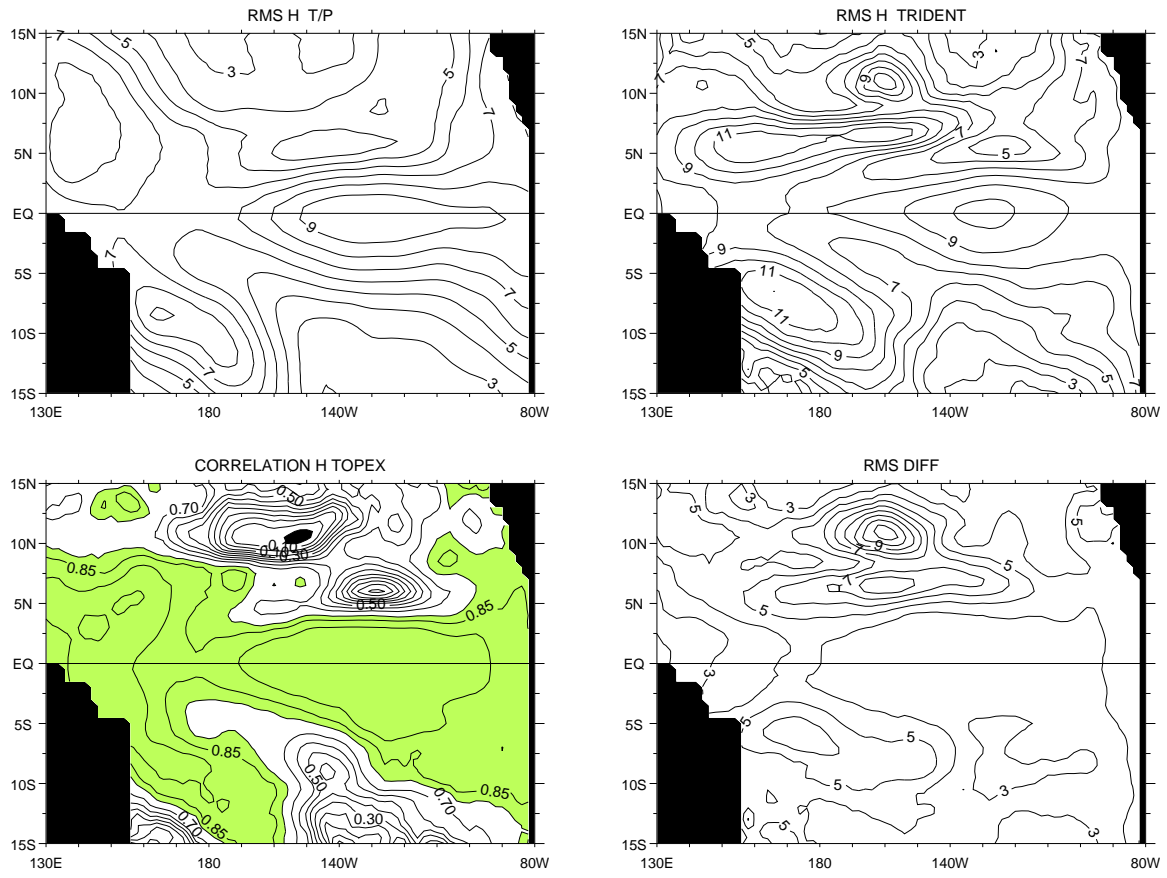
Figure 2:

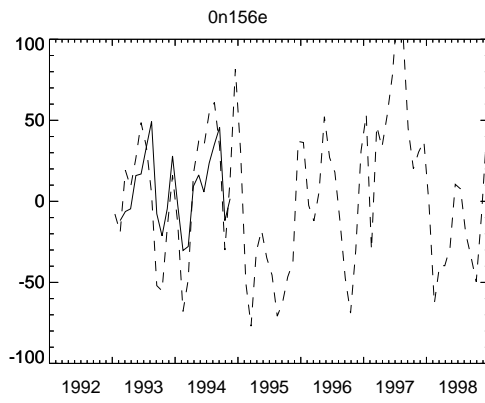Figure 3:

Figure 4:
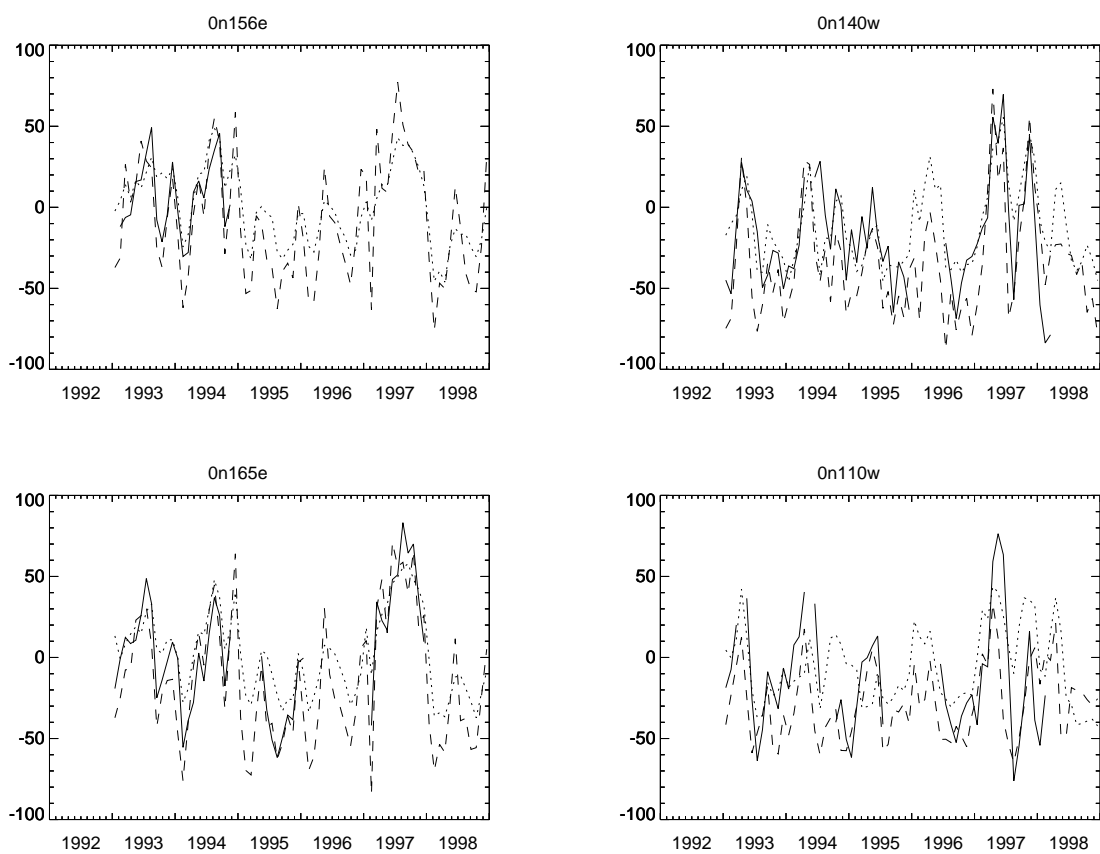
Figure 5:
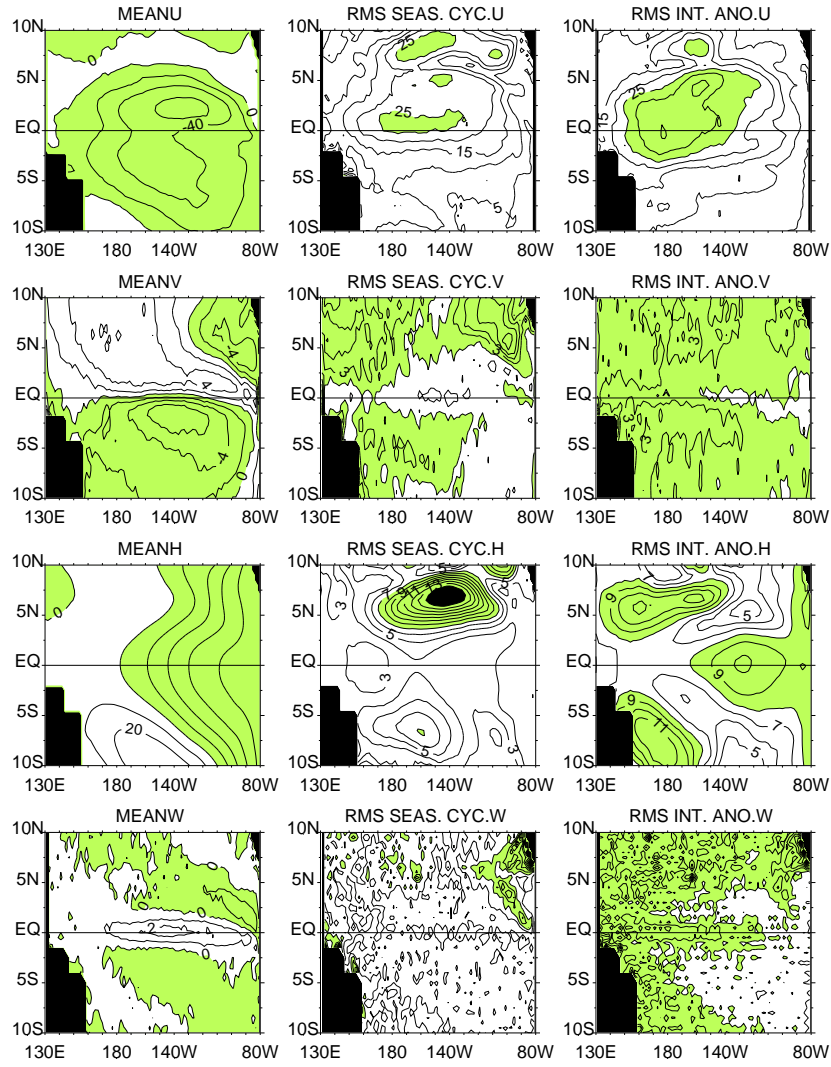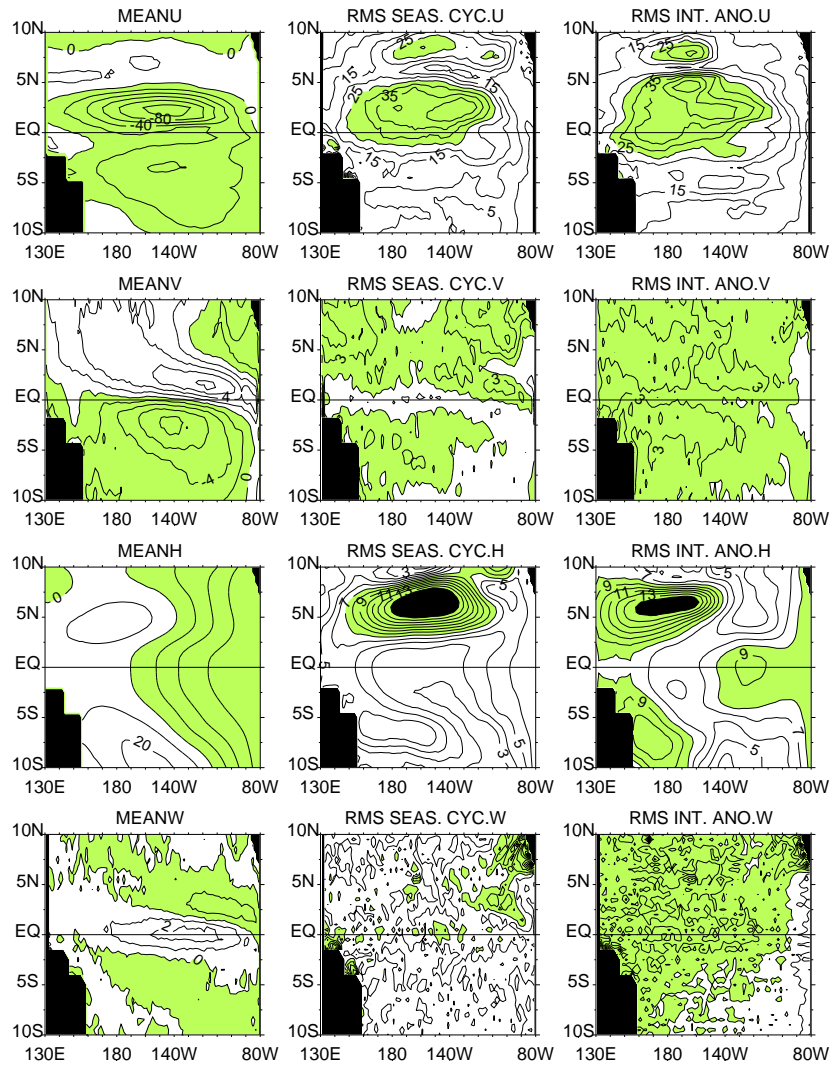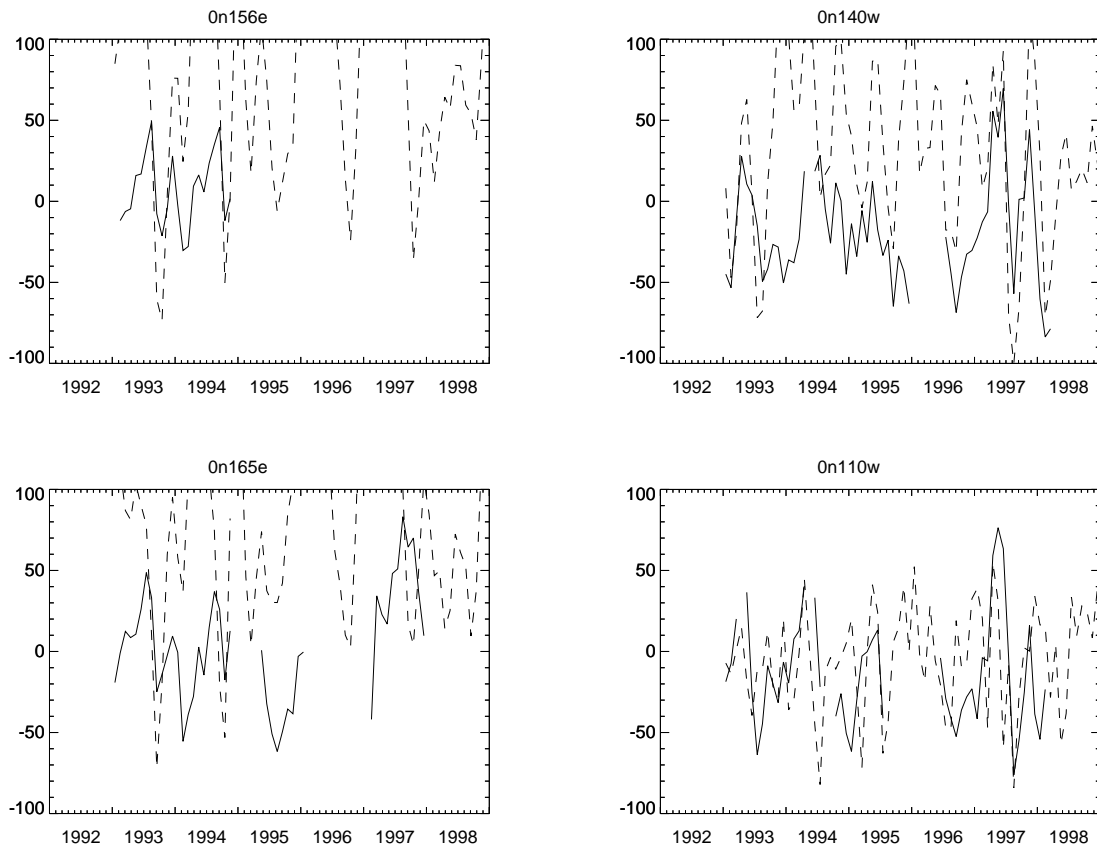
Figure 6:
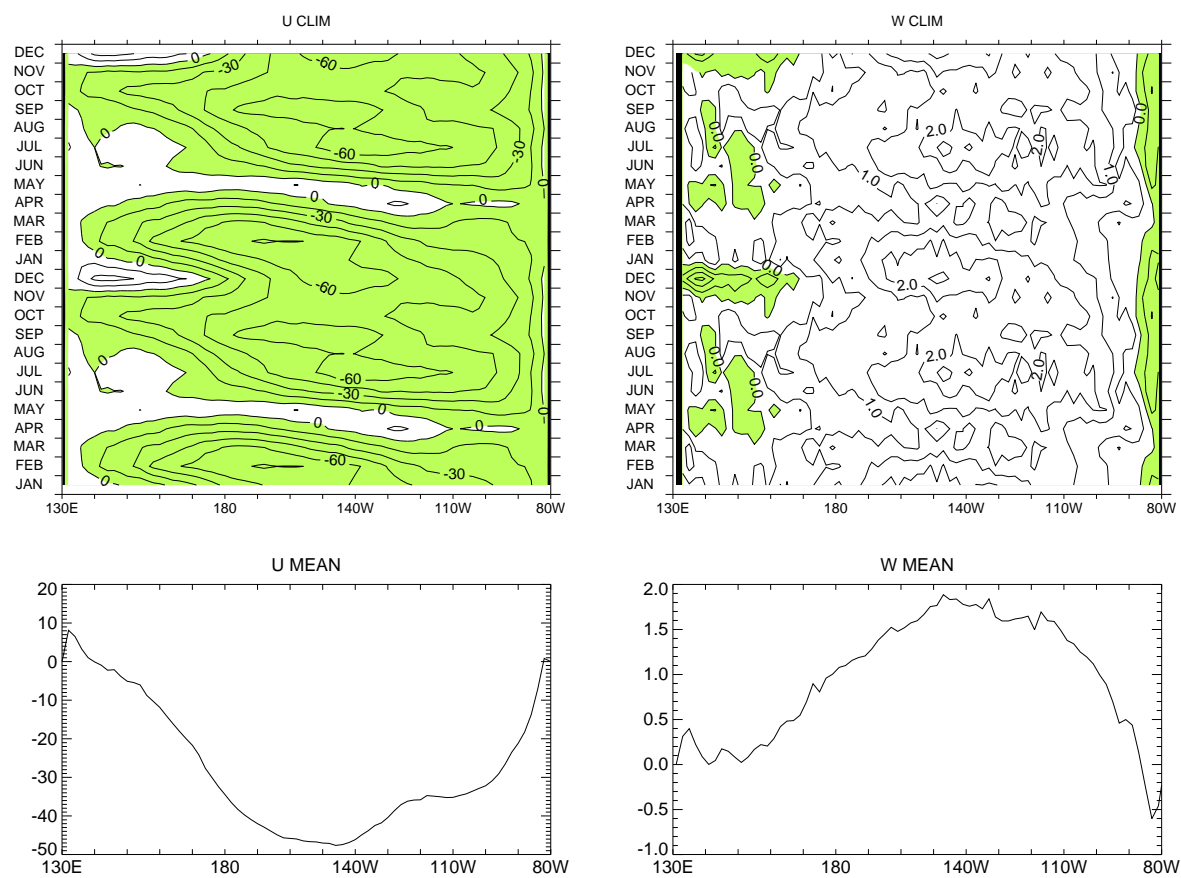
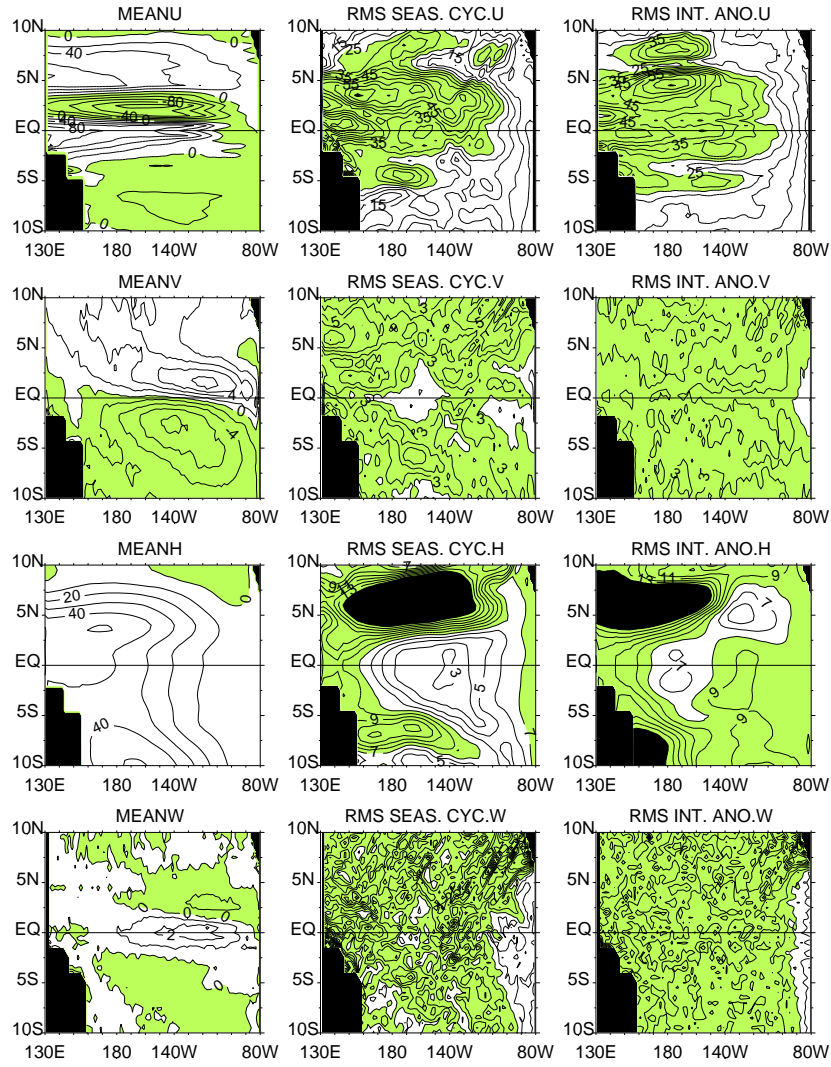Figure 7:
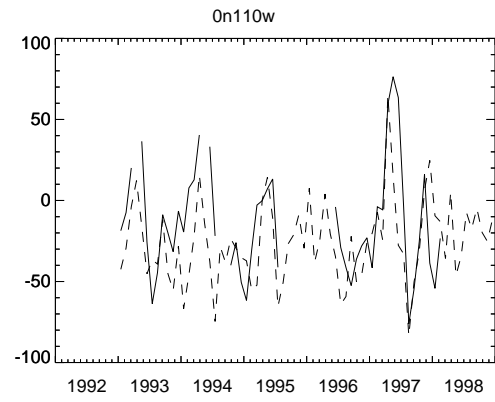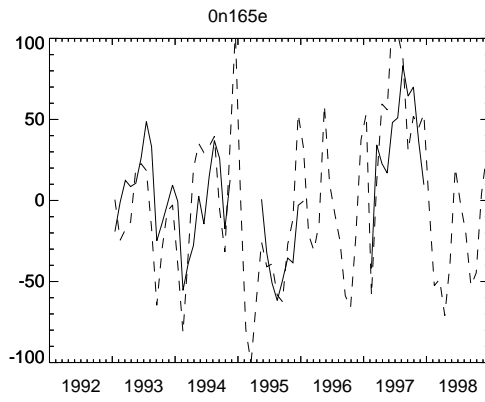
Figure 8:

Figure 9:

Figure 10:

Figure 11:

Déjà paru :

3 : Février 1998 Valérie Masson, Sylvie Joussaume, Sophie Pinot and Gilles Ramstein, *Impact of parameterizations on simulated winter mid-Holocene and Last Glacial Maximum climatic changes in the Northern Hemisphere*

4 : Mars 1998 Jérôme Vialard et Pascale Delecluse, *An OGCM Study for the TOGA Decade. Part I: Role of Salinity in the Physics of the Western Pacific Fresh Pool, Part II: Barrier layer formation and variability*

5 : Avril 1998 O. Aumont, J. C. Orr, P. Monfray, and G. Madec, *Nutrient trapping in the equatorial Pacific: The ocean circulation solution*

6 : Mai 1998 Emmanuelle Cohen-Solal and Hervé Le Treut, *Long term climate drift of a coupled surface ocean-atmosphere model : role of ocean heat transport and cloud radiative feedbacks*

7 : Juin 1998 Marina Lévy, Laurent Mémery and Gurvan Madec, *Combined Effects of Mesoscale Processes and Atmospheric High-Frequency Variability on the Spring Bloom in the MEDOC Area*

8 : Septembre 1998 Carine Laurent, Hervé Le Treut, Zhao-Xin Li, Laurent Fairhead and Jean-Louis Dufresne, *The influence of resolution in simulating inter-annual and inter-decadal variability in a coupled ocean-atmosphere GCM, with emphasis over the North Atlantic.*

9 : Octobre 1998 Francis Codron, Augustin Vintzileos and Robert Sadourny, *An Improved Interpolation Scheme between an Atmospheric Model and Underlying Surface Grids near Orography and Ocean Boundaries.*

10 : Novembre 1998 Z.X. Li and A.F. Carril, *Transient properties of atmospheric circulation in two reanalysis datasets.*

11 : Décembre 1998 Gurvan Madec, Pascale Delecluse, Maurice Imbard and Claire Lévy, *OPA8.1 ocean general circulation model reference manual.*

12 : Janvier 1999 Marc Guyon, Gurvan Madec, François-Xavier Roux, Christophe Herbaut, Maurice Imbard, and Philippe Fraunie*Domain Decomposition Method as a Nutshell for Massively Parallel Ocean Modelling with the OPA Model .*

13 : Février 1999 Eric Guilyardi, Gurvan Madec, and Laurent Terray *he Role of Lateral Ocean Physics in the Upper Ocean Thermal Balance of a Coupled Ocean-Atmosphere GCM*

14 : Mars 1999 D. Hauglustaine *Impact of Biomass Burning and Lightning Emissions on the Distribution of Tropospheric Ozone and its Precursors in the Tropics*

15 : Décembre 1999 L. Menut, R. Vautard, C. Honnoré, and M. Beekmann *Sensitivity of Photochemical Pollution using the Adjoint of a Simplified Chemistry-Transport Model*

16 : Janvier 2000 J.-Ph. Boulanger *The Trident Pacific model. Part 1: The oceanic dynamical model and observations during the TOPEX/POSEIDON period*

Plus de détails sont disponibles sur Internet :
http://www.ipsl.jussieu.fr/modelisation/liste-notes.html.